


Aortic 4D flow MRI in 2 minutes using compressed sensing, respiratory controlled adaptive k-space reordering, and inline reconstruction

Liliana E. Ma^{1,2}  | Michael Markl^{1,2} | Kelvin Chow^{1,3} | Hyungkyu Huh⁴ |
Christoph Forman⁵ | Alireza Vali¹ | Andreas Greiser⁵ | James Carr¹ |
Susanne Schnell¹ | Alex J. Barker^{6,7} | Ning Jin⁸

¹Department of Radiology, Feinberg School of Medicine, Northwestern University, Chicago, Illinois

²Department of Biomedical Engineering, Northwestern University, Chicago, Illinois

³Cardiovascular MR R&D, Siemens Medical Solutions USA, Inc, Chicago, Illinois

⁴Daegu-Gyeongbuk Medical Innovation Foundation, Medical Device Development Center, Daegu, South Korea

⁵Siemens Healthcare, Erlangen, Germany

⁶Department of Radiology, Children's Hospital Colorado, University of Colorado, Anschutz Medical Campus, Denver, Colorado

⁷Department of Bioengineering, University of Colorado, Anschutz Medical Campus, Denver, Colorado

⁸Cardiovascular MR R&D, Siemens Medical Solutions USA, Inc, Cleveland, Ohio

Correspondence

Ning Jin, 737 North Michigan Avenue,
Chicago, IL 60611.
Email: ning.jin@siemens-healthineers.com

Funding information

Research reported in this publication was supported by the National Heart, Lung, and Blood Institute of the NIH under Award Nos. F30HL137279, R01HL115828, R01HL133504, K25HL119608, the National Institute of Neurological Disorders and Stroke (NIH) 1R21NS106696, and by the American Heart Association under award 16SDG30420005.

Purpose: To evaluate the accuracy and feasibility of a free-breathing 4D flow technique using compressed sensing (CS), where 4D flow imaging of the thoracic aorta is performed in 2 min with inline image reconstruction on the MRI scanner in less than 5 min.

Methods: The 10 in vitro 4D flow MRI scans were performed with different acceleration rates on a pulsatile flow phantom (9 CS acceleration factors [$R = 5.4\text{--}14.1$], 1 generalized autocalibrating partially parallel acquisition [GRAPPA] $R = 2$). Based on in vitro results, CS-accelerated 4D flow of the thoracic aorta was acquired in 20 healthy volunteers (38.3 ± 15.2 years old) and 11 patients with aortic disease (61.3 ± 15.1 years) with $R = 7.7$. A conventional 4D flow scan was acquired with matched spatial coverage and temporal resolution.

Results: CS depicted similar hemodynamics to conventional 4D flow in vitro, and in vivo, with >70% reduction in scan time (volunteers: $1:52 \pm 0:25$ versus $7:25 \pm 2:35$ min). Net flow values were within 3.5% in healthy volunteers, and voxel-by-voxel comparison demonstrated good agreement. CS significantly underestimated peak velocities (v_{\max}) and peak flow (Q_{\max}) in both volunteers and patients (volunteers: v_{\max} , -16.2% to -9.4% , Q_{\max} : -11.6% to -2.9% , patients: v_{\max} , -11.2% to -4.0% ; Q_{\max} , -10.2% to -5.8%).

Conclusion: Aortic 4D flow with CS is feasible in a two minute scan with less than 5 min for inline reconstruction. While net flow agreement was excellent, CS with $R = 7.7$ produced underestimation of Q_{\max} and v_{\max} ; however, these were

generally within 13% of conventional 4D flow-derived values. This approach allows 4D flow to be feasible in clinical practice for comprehensive assessment of hemodynamics.

KEYWORDS

4D flow, aorta, cardiovascular, compressed sensing

1 | INTRODUCTION

3D cine phase-contrast MRI with 3-directional velocity encoding (also known as “4D flow MRI”) enables quantification and visualization of blood flow dynamics in the 3D volume over the cardiac cycle. Advantages of 4D flow MRI compared with standard techniques such as 2D phase contrast (PC) MRI or Doppler echocardiography include the visualization of complex cardiovascular 3D hemodynamics and retrospective flow quantification at any location in the data volume.¹⁻⁴ Several studies have shown that 4D flow MRI can provide new insights into the relationship between 3D hemodynamics and the development of aortic pathologies. For example, recent 4D flow MRI studies have shown that bicuspid aortic valve (BAV)-mediated changes in aortic hemodynamics are associated with aortic dilatation and aortic wall degeneration as observed by tissue histopathology, suggesting a physiologic mechanism by which valve abnormalities can influence the development of aortic disease.⁵⁻⁹ However, clinical applications are still limited by long scan times associated with multidimensional imaging (3D spatial and 3-directional velocity-encoding, time-resolved over the entire cardiac cycle).

Parallel imaging techniques, such as generalized autocalibrating partially parallel acquisition (GRAPPA) and sensitivity encoding technique (SENSE), are commonly used in 4D flow imaging to provide 2- to 3-fold acceleration; however, these techniques still result in scan times of 5-15 min. Recent and ongoing developments in advanced imaging techniques have further reduced scan times, by (1) incorporating radial sampling patterns (PC-VIPR¹⁰), (2) exploiting spatio-temporal correlations (k-t SENSE, k-t BLAST¹¹, and PEAK-GRAPPA¹²) to achieve acceleration rates of $R \sim 5$, and (3) using sparse sampling patterns (e.g., k-t PCA¹³) to push acceleration rates even further.

In the past decade, compressed sensing (CS), which exploits the inherent compressibility of MRI data, has been combined with parallel imaging to achieve even higher acceleration rates, enabling 4D flow scan times to become clinically feasible.¹⁴⁻²³ To date, several preliminary studies have reported the application of CS to 4D flow imaging using a variety of sampling patterns. Dyvorne et al achieved acceleration factors of 6, using a spiral sampling pattern to achieve 4D flow coverage of the abdomen in a single breathhold,²⁴ Hsiao et al successfully applied a variable-density Poisson-disk

Cartesian sampling pattern to a pediatric population,²⁵ and more recently, Cheng et al combined variable-density cartesian sampling with radial view-ordering (VDRad) and CS to achieve acceleration factors of ~ 10.6 . However, while the results of these studies have shown significant improvements in scan time, they were limited by offline reconstruction times, usually on the order of 3+ h, making implementation into most clinical workflows difficult.

Here, we propose a prototype 4D flow technique using Respiratory Controlled Adaptive k-space Reordering (ReCAR) combined with a variable-density phyllotaxis pattern for subsampling and L1-regularized wavelet-based compressed sensing for image reconstruction. This approach allows 4D flow imaging of the thoracic aorta to be performed in 2 min with inline image reconstruction on the MRI system platform in less than 5 min. The purpose of this study was to systematically investigate the accuracy and feasibility of CS-accelerated 4D flow MRI with comparison to conventional 4D flow using in vitro flow phantom experiments and in vivo studies in healthy volunteers and patients with aortic valve disease.

2 | METHODS

2.1 | CS-accelerated 4D flow MRI

Pulse Sequence: A CS-accelerated 4D flow MRI sequence was implemented using retrospective electrocardiographic-gating and symmetric, 4-point velocity encoding (Figure 1A). 4D flow data were acquired during free breathing using navigator-gating and ReCAR, where the diaphragm position was used to acquire central k-space at end-expiration and peripheral k-space during inspiration (Figure 1C).^{26,27} This technique included a previously described, variable-density, Cartesian spiral phyllotaxis sampling pattern, with sampling patterns rotated between successive cardiac time frames to form a fully sampled center for coil-sensitivity estimation,²⁸ for use in the reconstruction.²⁹ All scans were acquired on a 1.5T system (MAGNETOM Aera, Siemens Healthcare, Erlangen, Germany).

2.1.1 | Image reconstruction

Inline CS reconstruction was implemented based on a previously described framework³⁰ by solving the following optimization problem:

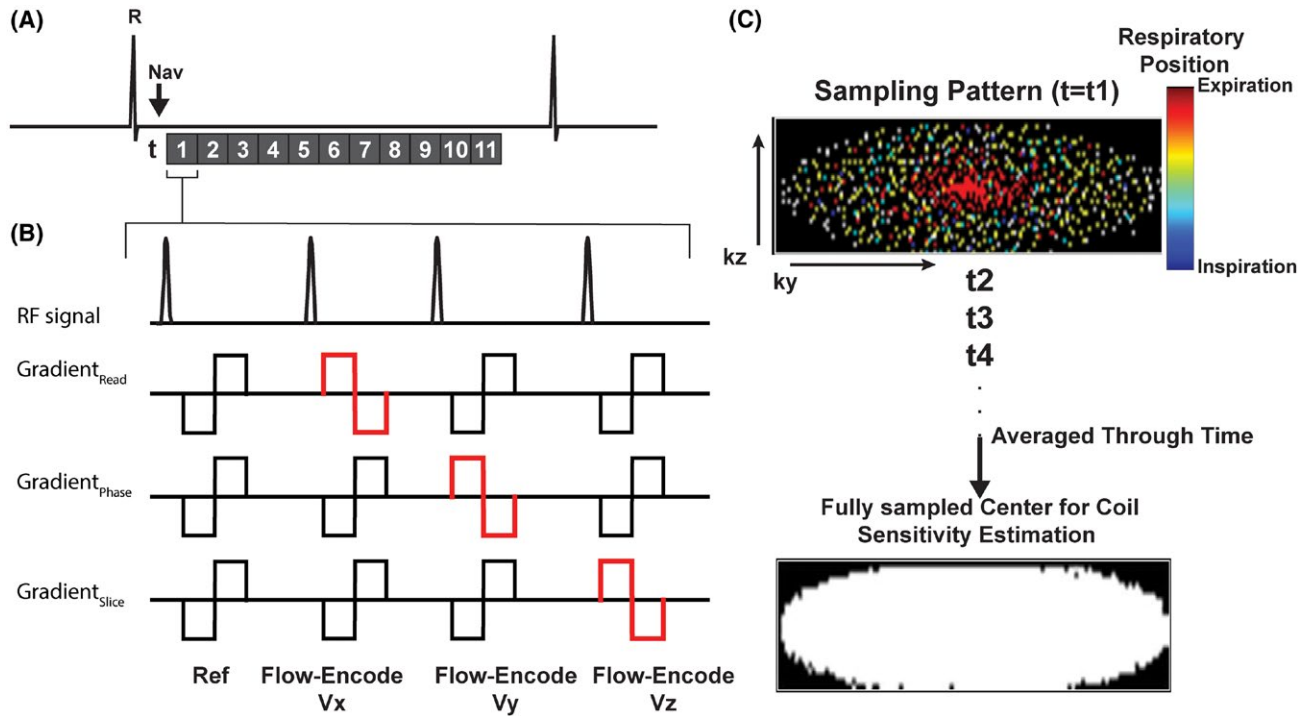


FIGURE 1 CS acquisition and reconstruction. A,B, Retrospectively-gated flow acquisition using symmetric 4-point encoding gated to the cardiac cycle. Only bipolar flow gradients are depicted. Imaging gradients are not included for simplicity. Navigator echoes (Nav) were played out after R-wave detection in the ECG tracing. Numbers (1-11) represent successive cardiac time frames (t_n , $n = 1, 2, \dots, 11$). In each cardiac phase, a segment of k-space (views per segment = 2) is acquired. C, ReCAR with combined with spiral phyllotaxis subsampling pattern in the kz/ky dimensions of a single time frame, that is subsequently rotated for each time frame (t_n). Central k-space is acquired during expiration (red) and outer k-space is acquired during inspiration (blue) to mitigate respiratory motion artifacts. When all cardiac time frames are combined, they form a fully sampled center of k-space, (D), for coil sensitivity estimation

$$\{\mathbf{x}_t\}_{t=1, \dots, T} = \underset{\{\mathbf{x}_t\}}{\operatorname{argmin}} \sum_{t=1}^T (\|\mathbf{A}_t \mathbf{x}_t - \mathbf{y}_t\|_2^2 + \lambda_\sigma \|\mathbf{W}_\sigma \mathbf{x}_t\|_1) + \lambda_\tau \|\mathbf{W}_\tau \{\mathbf{x}_1^T, \dots, \mathbf{x}_T^T\}\|_1^T \quad (1)$$

where \mathbf{x}_t denotes the frames to be reconstructed for all time points, \mathbf{A}_t is the system matrix for each time point, t , consisting of the Fourier transform, sampling pattern, and coil sensitivity profiles for the local receiver coil elements and \mathbf{y}_t denotes the measured data for each time point. Spatio-temporal L1 regularization was performed using a Haar wavelet transform where \mathbf{W}_σ and \mathbf{W}_τ represent spatial and temporal Wavelet transforms, and λ_σ and λ_τ the spatial and temporal regularization parameters, respectively. Equation 1 was solved using a FISTA³¹ optimization, and the reconstruction was fully integrated on a standard clinical scanner reconstruction system equipped with 2 graphics processing units (Tesla K10).³² The reconstruction parameters included 30 FISTA iterations with, $\lambda_\sigma = 0.0015$ and $\lambda_\tau = 5\lambda_\sigma$, assuming a maximum image magnitude intensity equal to 1. The regularization parameter, λ_σ , was scaled to the maximum image intensity, or $\lambda_{\sigma, \text{actual}} = \lambda_\sigma * \max(|\text{image}|)$.

2.2 | In vitro flow phantom experiments

2.2.1 | Pulsatile flow circuit and flow phantom

CS 4D flow MRI was systematically evaluated in an in vitro flow phantom using an MRI-compatible pulsatile flow circuit, and a patient-based 3D-printed realistic aorta flow phantom with an 80% coarctation in the descending aorta as described previously.³³ Briefly, realistic pulsatile flow was generated using a pneumatically driven ventricular assist device (VAD) and pump control unit (MEDOS, Germany). The pump control unit supplied the pressure from outside the MR room. The VAD was directly attached to the 3D printed patient-specific model to mimic pulsatile flow entering the thoracic aorta and used to generate flow rates of up to 3.5 L/s at frequencies of 69 “beats” per minute. Water doped with gadolinium-based contrast material was used as fluid in all experiments. All in vitro 4D flow measurements were gated to the pulsatile flow by a trigger signal generated by the pump control unit.

2.2.2 | In vitro phantom measurements

A total of 10 in vitro 4D flow MRI scans were performed (one conventional GRAPPA-accelerated 4D flow scan with $R = 2$ and CS accelerated 4D flow with 9 different acceleration factors, $R = 5.4$ -14.1). CS accelerated and conventional 4D flow MRI data were acquired with the following identical sequence parameters: TE/TR = 2.1/4.8 ms, BW = 455 Hz/voxel, flip angle = 15° , spatial resolution = 2.3 mm^3 , velocity encoding (Venc) = 350 cm/s, temporal resolution = 39 ms, 22 cardiac time frames.

2.2.3 | In vitro data analysis

4D flow MRI data preprocessing included noise-filtering, correction for Maxwell terms and second-order eddy current correction.³⁴⁻³⁶ A 3D phase contrast MR angiogram (PC-MRA) was calculated from the 4D flow data and used to create a 3D segmentation of the thoracic aorta phantom (Mimics, Materialise, Leuven, Belgium). For both CS and non-CS acquisitions, nine 2D analysis planes were placed orthogonally along the entire aorta for quantification of regional peak velocities (v_{\max}) and time-resolved flow (Figure 2Aa). To visualize systolic blood flow in the entire aorta, systolic velocity

maximum intensity projections (MIPs) were created by projecting the maximum velocity magnitude (speed) onto a sagittal-oblique plane through the thoracic aorta (Figure 2A).³⁷ Cross-vessel line profiles were drawn through planes Root, AAo2, Arch3, DAo1, and DAo3 to evaluate the effects of CS spatial regularization at end diastolic and peak systolic time frames (Figure 3A). The CS data were temporally interpolated, using a spline interpolation, to the corresponding conventional 4D flow scan and voxel-by-voxel comparison of the CS versus conventional 4D flow scans was performed using velocity magnitude, $|v|$, where $|v| = \sqrt{v_x^2 + v_y^2 + v_z^2}$.

2.3 | In vivo CS 4D flow study

2.3.1 | Study cohort

CS-accelerated and conventional 4D flow MRI of the thoracic aorta was prospectively acquired in 20 healthy volunteers (age = 38.3 ± 15.2 years old; range: 20-70 years; 10M/10F) and 11 patients with aortic valve disease (age = 61.3 ± 15.1 years; range: 27-79 years; 9M/2F) from January to September 2018. 4D flow was acquired in all volunteers without contrast. Two patients were imaged after aortic valve replacement, 5 patients had BAV disease, 2 patients had

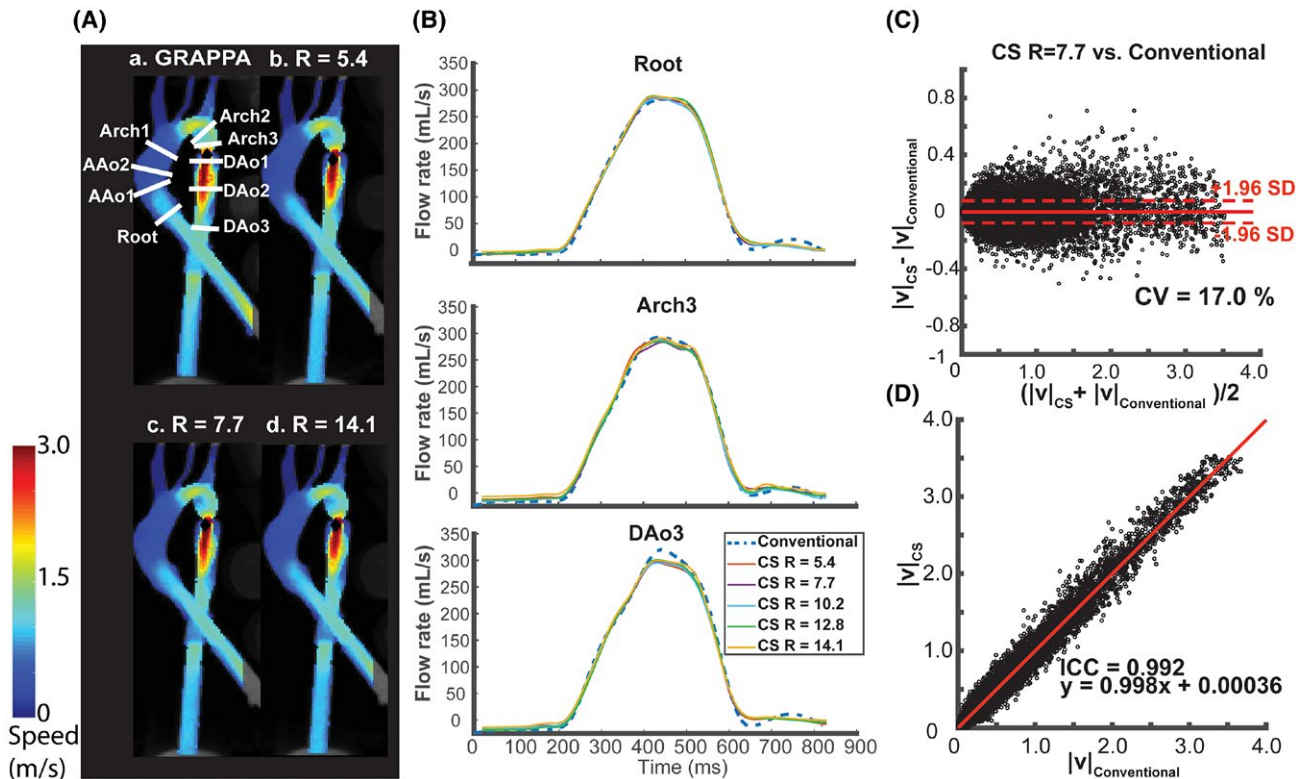


FIGURE 2 In vitro 3D printed aorta flow phantom analysis. A, Systolic velocity maximum intensity projections (MIPs) of conventional 4D flow (a) compared with CS accelerated 4D flow MRI with three representative acceleration factors (b-d). Locations of 9 2D analysis planes for quantification of v_{\max} and flow-time curves and flow time curves are shown in (a). B, Representative flow curves at three locations in the aorta for conventional 4D flow (dashed blue line, GRAPPA, $R = 2$) compared with CS accelerated 4D flow with 5 different acceleration factors ranging from $R = 5.4$ - 14.1. C, Voxel-by-voxel Bland-Altman comparison of absolute velocities in the entire aorta phantom between CS accelerated 4D flow with $R = 7.7$ versus conventional 4D flow. D, Voxel-by-voxel orthogonal regression analysis between CS accelerated 4D flow with $R = 7.7$ and conventional 4D flow

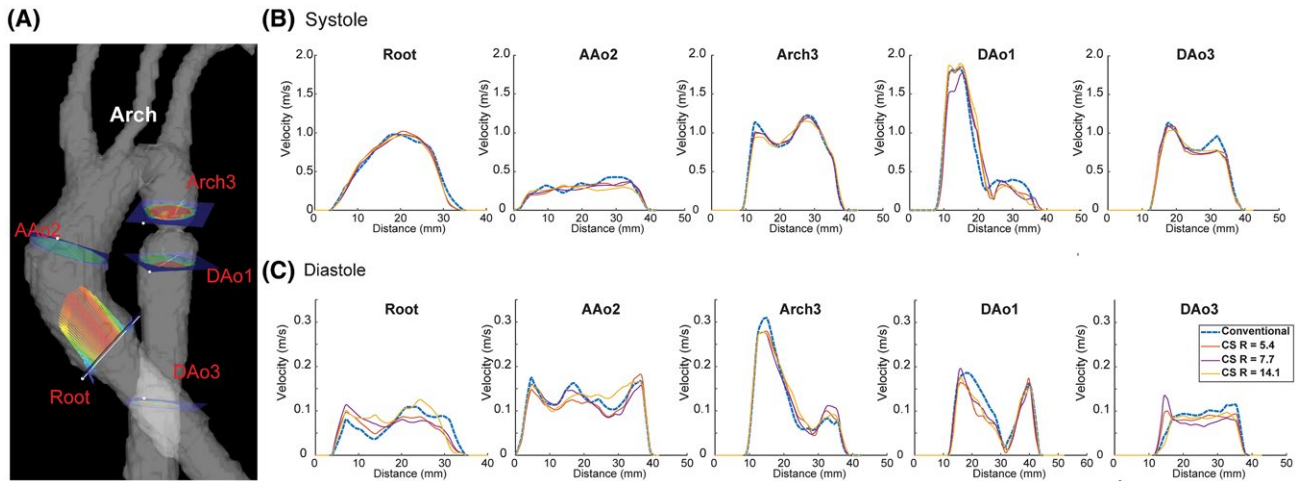


FIGURE 3 In vitro 3D printed aorta flow phantom velocity profiles. A, Planes at which cross-sectional lines were drawn for evaluation of velocity profiles. The plane at the Root shows velocity vectors along the cross-vessel line. The magnitude of the velocity vector along the line was plotted for 5 planes. B, Velocity profiles for five planes and three representative CS acceleration factors. Note the blunting of CS peaks for all acceleration factors in AAo2, Arch3, and DAo3 which seems to be more severe for $R = 14.1$ in systole. C, Velocity profiles in end diastole. Some blunting of velocity profiles is also seen in AAo2, Arch3, and DAo3

aortic stenosis, 1 patient had moderate to severe aortic insufficiency, and 1 patient had aortic root enlargement with trace regurgitation. The study was approved by the Institutional Review Board of Northwestern University. Written informed consent was obtained from all volunteers and patients. Six of 11 patients underwent standard-of-care cardiothoracic MRI including contrast agent administration (Gadavist, Bayer Healthcare) and conventional 4D flow MRI (after contrast injection). Informed consent was obtained in these patients for the additional CS 4D flow acquisition.

2.3.2 | In vivo data acquisition

For all subjects, a retrospectively-gated CS accelerated 4D flow sequence was acquired with an acceleration rate (R) of 7.7 (identified as optimal R based on phantom experiments). For comparison, a conventional, retrospectively-gated 4D flow sequence with $R = 2$ GRAPPA acceleration with matched spatial/temporal resolution was acquired immediately after the CS accelerated 4D flow scan, or before in the case of the six patients who received 4D flow as part of their standard-of-care imaging. Pulse sequence parameters are summarized in Table 1.

2.3.3 | In vivo data analysis

The same preprocessing workflow applied to phantom images was applied to in vivo data, with a first-order eddy current correction, and correction for velocity aliasing when necessary.^{33,36} A 4D flow-derived 3D PC MR angiogram was used to generate a 3D segmentation of the thoracic aorta. For regional flow quantification, nine 2D analysis planes were

placed orthogonally along the entire aorta at the following anatomic landmarks: “Root” placed at the aortic root, AAo1 and AAo2 spaced evenly between the Root and Arch1 plane, which was placed just before the brachiocephalic trunk; Arch2 placed just past the left subclavian artery, with Arch3 and DAo1-3 spaced evenly down the distal arch and descending aorta (Figure 4A, top right).

To account for the slightly different temporal resolutions of CS accelerated and conventional 4D flow MRI, all flow curves were interpolated to a temporal resolution of 10 ms. Aortic velocity MIPs were calculated and used to visualize blood flow (Figure 4IA, IIA), as well as to quantify peak systolic velocities (v_{\max}) in 3 selected regions of interest in all subjects: the ascending aorta (AAo, defined from the aortic root to before the brachiocephalic trunk [BCT]), aortic arch (arch), and descending aorta (DAo) (Figure 4A, top left). Time-resolved 3D streamlines (Ensight, CEI, Apex, NC) were also generated to visualize blood flow (Figure 4B). CS and conventional 4D flow scans were acquired consecutively with the same spatial imaging coverage, and their respective segmentations were visually inspected for agreement for a voxel-by-voxel analysis (see Supporting Information Figure S1, which is available online). Voxel-by-voxel comparison of the CS $R = 7.7$ and conventional 4D flow scans was performed for each subject in the same manner as the in vitro phantom comparison.

2.4 | Statistical analysis

All numbers are reported as mean \pm standard deviation (SD) or percentages relative to conventional 4D flow values. The flow-time curves in all nine 2D analysis planes were averaged

TABLE 1 4D flow imaging parameters for all volunteers and patients

	Conventional	CS
Acceleration rate, R	2	7.7
Scan time (s)	460 ± 218 (433 ± 159)	116 ± 18 (110 ± 25)
Echo time (ms)	2.3 (2.0–2.3)	2.3 (2.0–2.3)
Repetition time	5.1 (4.8–5.1)	5.1 (4.8–5.1)
Temporal resolution (ms)	40.0–45.3	38.1–44.5
BW	455	455
Flip angle (°)	7 (15 with contrast)	7 (15 with contrast)
Interpolated voxel size (mm ³)	2.4–2.5 × 2.4–2.5 × 2.4–2.9	2.4–2.5 × 2.4–2.5 × 2.4–2.9
Acquired voxel size (mm ³)	2.4–2.5 × 3.5–3.8 × 3.6–4.3	2.4–2.5 × 3.5–3.8 × 3.3–3.8
Acquired matrix size	160 × 82 × 20	160 × 82 × 20
Field of view (mm ³)	380–400 × 285–315 × 72–84	380–400 × 285–315 × 72–84
Venc (cm/s)	150 (150–500)	150 (150–500)
Reconstructed cardiac phases	18–32	17–31
Navigator acceptance Window (mm)	±8	±8

Notable differences in patient parameters are represented in parentheses.

over all 20 volunteers for comparison of flow quantification. A Lilliefors test was used to evaluate parameter normality, and a nonparametric Wilcoxon rank-sum (RS) or a 2-tailed, paired t-test was used accordingly to evaluate for differences between continuous parameters. Voxel-by-voxel comparisons included Bland-Altman analysis to establish the mean difference and limits of agreement (LOA) between the 4D flow techniques and calculation of a coefficient of variation (CV). Correlation between the 2 methods was assessed using orthogonal regression, with further evaluation using the intraclass correlation coefficient (ICC). A *P*-value < 0.05 was considered statistically significant.

3 | RESULTS

3.1 | In Vitro

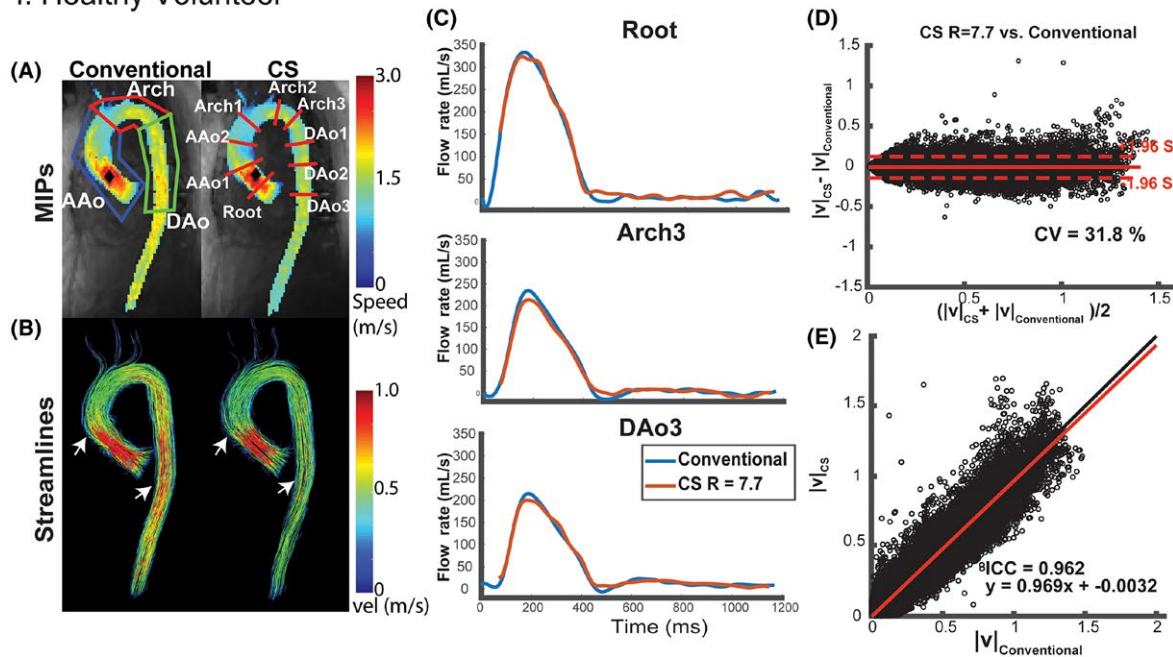
Phantom results are summarized in Figures 2 and 3 and Table 2. Systolic velocity MIPs in a sagittal orientation for three representative CS acceleration factors (*R* = 5.4; *R* = 7.7; and *R* = 14.1; Figure 2A) demonstrate good visual agreement with conventional (GRAPPA; *R* = 2) in vitro 4D flow MRI. Flow quantification at representative 2D analysis planes (Figure 2B) depict similar flow curve shapes between techniques, with noticeable but mild underestimation of peak flow (*Q*_{max}) in the CS acquisition, which was most perceptible in the descending aorta (DAo3). As delineated in Table 2, relative change in *Q*_{max} (% differences between CS accelerated and conventional 4D flow MRI) across all 9 acceleration factors was Root: 0.5% to 2.7%, AAo (2 planes): −12.6% to −4.3%, Arch (3 planes): −13.1% to −0.4%, DAo

(3 planes): −9.5% to 1.2%. *v*_{max} quantified over the nine 2D analysis planes also showed an underestimation compared with conventional 4D flow, varying with CS acceleration factor (Root: −9.3% to 3.7%, AAo : −22.5% to −5.1 %, Arch: −16.7% to −0.6%, Dao: −19.9% to 1.3%). The relative change in net flow (*Q*_{net}) in the entire aorta over all acceleration factors ranged from −10.0% to 7.6% (Table 2).

Figure 3 shows cross-vessel velocities for peak systole (time point with the highest *v*_{max}) and end diastole for 3 representative acceleration factors. CS 4D flow demonstrates good agreement with conventional 4D flow (similar velocity profiles in systole and diastole), with some blunting of peaks along a cross-vessel line in most systolic planes as well as in AAo2, Arch3, and DAo3 in diastole.

Figure 2C,D shows Bland-Altman voxel-by-voxel comparisons and correlation plots for absolute aortic velocities for one representative acceleration factor (*R* = 7.7) versus conventional 4D flow MRI (GRAPPA with *R* = 2). Bland-Altman (Figure 2C) and correlation analysis (Figure 2D) indicate good-excellent agreement between both techniques as summarized in Supporting Information Table S1, which includes findings for experiments with all 9 acceleration factors. Bland-Altman analysis revealed mean differences with a small negative bias (<0.01 m/s) and good limits of agreement (<0.09 m/s) with respect to the mean velocities. In addition, ICCs indicate a strong correlation between the techniques with high ICC (0.990–0.993) and slope close to unity (0.98–1.00). While voxel-by-voxel comparisons are only presented for the magnitude of the velocity (speed), this analysis was performed for the separated velocity components (*x*, *y*, *z*) as well, leading to similarly

I. Healthy Volunteer



II. Prosthetic AV Patient

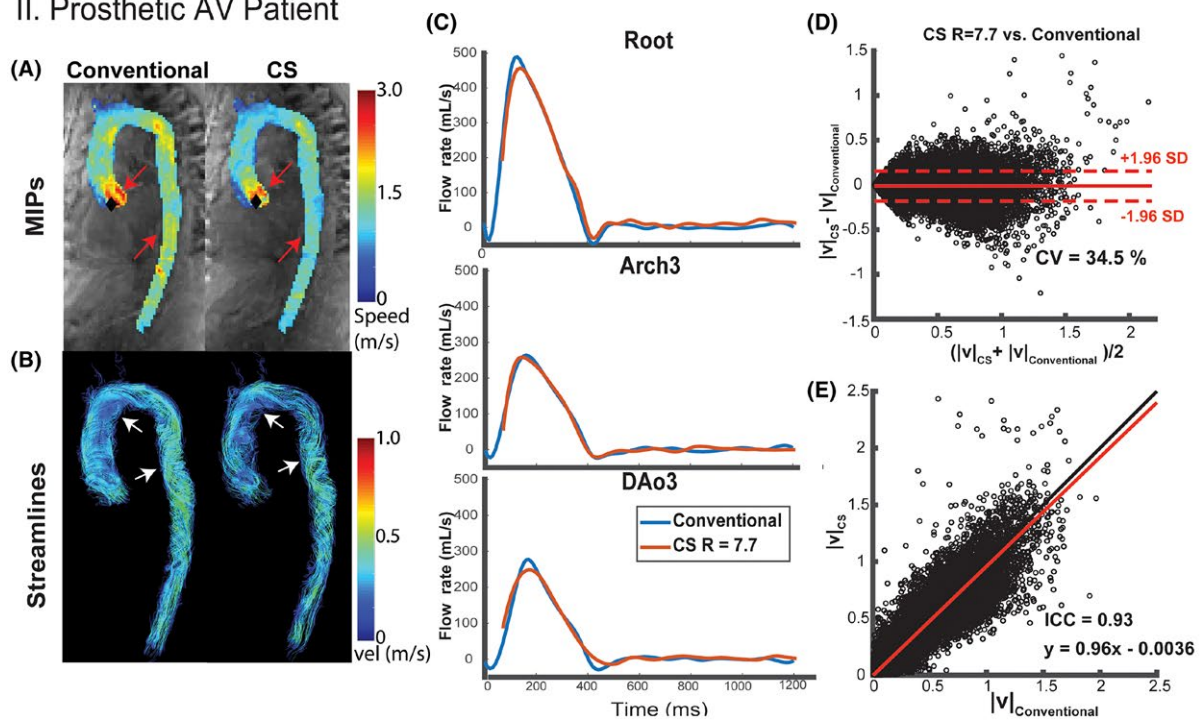


FIGURE 4 Representative in vivo aortic hemodynamics for a healthy volunteer (I) and patient (II). A, Peak velocity maximum intensity projections (MIPs, top) and systolic (I) or diastolic (II) 3D streamlines (bottom) of conventional 4D flow (GRAPPA, $R = 2$) and CS 4D flow ($R = 7.7$). Black diamonds represent points of maximum velocity in the MIPs. Regions of interest (I.A top left) were used to quantify v_{\max} in the ascending aorta (AAo), arch, and descending aorta (DAo). Nine 2D analysis planes at defined anatomic locations were used for flow quantification. Arrows indicate regions with visible differences between the 2 techniques. Note the underestimation in areas of high velocities in the ascending and descending aorta (white arrows). Prosthetic aortic valve (AV) patient diastolic streamlines depict complex helical flow in both techniques, with less dense streamlines in the CS accelerated 4D flow (red arrows). C, Representative flow curves at 3 locations in the aorta for conventional 4D flow (blue line) compared with CS accelerated 4D flow (red line). D, Voxel-by-voxel Bland-Altman comparison of absolute velocities in the entire aorta between CS accelerated 4D flow versus conventional 4D flow. E, Voxel-by-voxel orthogonal regression analysis between CS accelerated 4D flow with $R = 7.7$ versus conventional 4D flow

TABLE 2 In vitro study results

	Peak flow, Q_{\max} (mL/s for conventional GRAPPA, % for CS)								
	Root	AAo1	AAo2	Arch1	Arch2	Arch3	DAo1	DAo2	DAo3
GRAPPA R = 2	282.9	303.8	304.4	292.0	286.0	292.6	294.2	349.0	320.6
R = 5.4	0.5	−6.3	−9.5	−9.0	−5.1	−0.9	−5.5	−2.4	−7.8
R = 6.4	0.9	−5.1	−8.9	−9.4	−4.3	−0.9	−0.2	−5.8	−5.9
R = 7.7	1.0	−5.2	−9.6	−9.2	−6.6	−3.1	−2.7	−3.1	−7.2
R = 8.9	2.2	−5.8	−8.3	−7.3	−5.8	−2.6	−1.3	−7.5	−8.3
R = 10.2	0.7	−6.5	−4.7	−9.2	−7.1	−1.7	−0.4	−1.9	−7.9
R = 11.5	0.6	−6.4	−8.5	−7.7	−7.1	−3.2	−3.8	−4.4	−8.9
R = 12.8	2.4	−6.9	−12.6	−11.3	−6.6	−2.5	−3.2	−7.0	−6.1
R = 13.4	2.7	−6.7	−11.6	−11.7	−5.8	−2.7	−4.6	−9.5	−7.4
R = 14.1	2.1	−6.5	−12.2	−13.1	−6.8	−0.4	1.2	−6.0	−6.5

	Peak velocity, v_{\max} (m/s for conventional GRAPPA, % for CS)								
	Root	AAo1	AAo2	Arch1	Arch2	Arch3	DAo1	DAo2	DAo3
GRAPPA R = 2	1.08	0.78	0.49	0.48	1.53	1.56	3.16	2.25	1.46
R = 5.4	−3.7	−6.4	−14.3	−12.5	−1.3	−9.0	−0.3	−6.2	−13.0
R = 6.4	−5.6	−5.1	−22.4	−12.5	−0.7	−7.1	0.0	−11.6	−15.1
R = 7.7	−6.5	−12.8	−12.2	−8.3	−2.0	−10.3	−0.9	−7.6	−15.8
R = 8.9	−7.4	−9.0	−14.3	−6.2	−3.3	−10.9	1.3	−9.3	−15.1
R = 10.2	−7.4	−7.7	−12.2	−12.5	−3.3	−8.3	0.0	0.0	−19.2
R = 11.5	−9.3	−7.7	−20.4	−10.4	−3.9	−11.5	−4.4	−19.1	−19.2
R = 12.8	−5.6	−5.1	−10.2	−14.6	−5.2	−15.4	−5.1	−9.8	−19.9
R = 13.4	−7.4	−11.5	−14.3	−8.3	−4.6	−10.9	−5.1	−5.3	−19.2
R = 14.1	−8.3	−14.1	−22.4	−16.7	−4.6	−6.4	−4.7	−13.8	−19.9

	Net flow, Q_{net} (mL/cycle for conventional GRAPPA, % for CS)								
	Root	AAo1	AAo2	Arch1	Arch2	Arch3	DAo1	DAo2	DAo3
GRAPPA R = 2	75.8	80.9	84.9	83.7	74.0	71.6	67.5	87.2	74.4
R = 5.4	0.1	−3.6	−5.7	−2.5	−2.8	2.8	3.6	−6.0	−3.5
R = 6.4	−0.5	−3.6	−5.9	−3.5	−3.0	4.9	3.8	−10.0	−6.1
R = 7.7	0.1	−0.9	−1.6	−2.5	−3.4	−0.4	4.1	−4.9	−2.1
R = 8.9	0.2	1.4	2.2	5.5	−3.8	−1.4	1.0	−8.7	−2.4
R = 10.2	−0.5	−0.4	1.2	1.6	−4.5	−0.4	1.0	−5.3	−1.7
R = 11.5	1.8	2.8	1.4	2.5	−4.7	−0.5	2.8	−8.7	−3.5
R = 12.8	2.6	−0.8	−3.9	−2.0	−3.7	0.7	−1.5	−6.2	−2.4
R = 13.4	2.9	−0.3	−4.9	−2.7	−1.5	3.6	0.9	−8.5	−3.5
R = 14.1	2.8	−0.6	−7.3	−6.1	−1.7	6.7	7.6	−7.7	1.3

Peak flow, peak velocity, and net flow (top, middle, bottom) are presented for 9 different acceleration factors ranging from 5.4 to 14.1 (left column), for 9 different 2D analysis planes from the root to the descending aorta (top row). Conventional 4D flow parameters (GRAPPA R = 2) are presented in measurement units, CS 4D flow data for acceleration factors are presented as percentages relative to the conventional 4D flow-derived values.

low mean differences and limits of agreement (Supporting Information Table S2). An acceleration rate of $R = 7.7$ was reliable in producing results with an underestimation in Q_{\max} , v_{\max} , and a Q_{net} of <15% (except DAo3 v_{\max}), and thus this acceleration rate was subsequently chosen for the healthy control and patient cohorts.

3.2 | Healthy controls

All conventional 4D flow and CS 4D flow images were successfully acquired in all 20 healthy control subjects. The total scan time for in vivo CS 4D flow with $R = 7.7$ was significantly reduced compared with conventional 4D flow MRI

($1.56 \pm 0:18$ min versus $7:40 \pm 3:38$ min, $P < 0.001$), with inline image reconstruction for CS 4D flow in under 5 min. Representative blood flow visualization (systolic streamlines, velocity MIP), flow curves (Figure 4.I.C), and voxel-by-voxel Bland-Altman (Figure 4.I.D) composition shown in Figure 4 indicate similar hemodynamic patterns for CS and conventional in vivo 4D flow MRI (Figure 4.I). These findings were confirmed by quantitative comparisons of aortic in vivo flow and velocities as summarized in Figures 5 and 7 and Table 3. Flow-time curves for all 9 analysis planes (Figure 5) show good agreement between CS and conventional 4D flow MRI, but consistent with in vitro flow phantom findings,

significant differences (indicated by * in Figure 5) between techniques were concentrated at the peaks of the flow waveforms as well as at the transition to diastole. Time-resolved flow analysis revealed a significant decrease in Q_{\max} at the Root and in the Arch and DAo in the CS acquisition (Root: -7.6% , AAo: -8.7% to -2.9% , Arch: -9.0% to -7.8% , DAo: -11.6% to -8.4% , $P < 0.01$). Q_{net} of the CS acquisition were within 3.5% of those of the conventional 4D flow acquisition in all 9 2D analysis planes. Peak velocities calculated over the AAo, Arch, and DAo using MIPs, were significantly underestimated by CS compared with conventional 4D flow (Conventional, AAo: 1.55 ± 0.18 m/s, Arch: 1.21 ± 0.23 m/s,

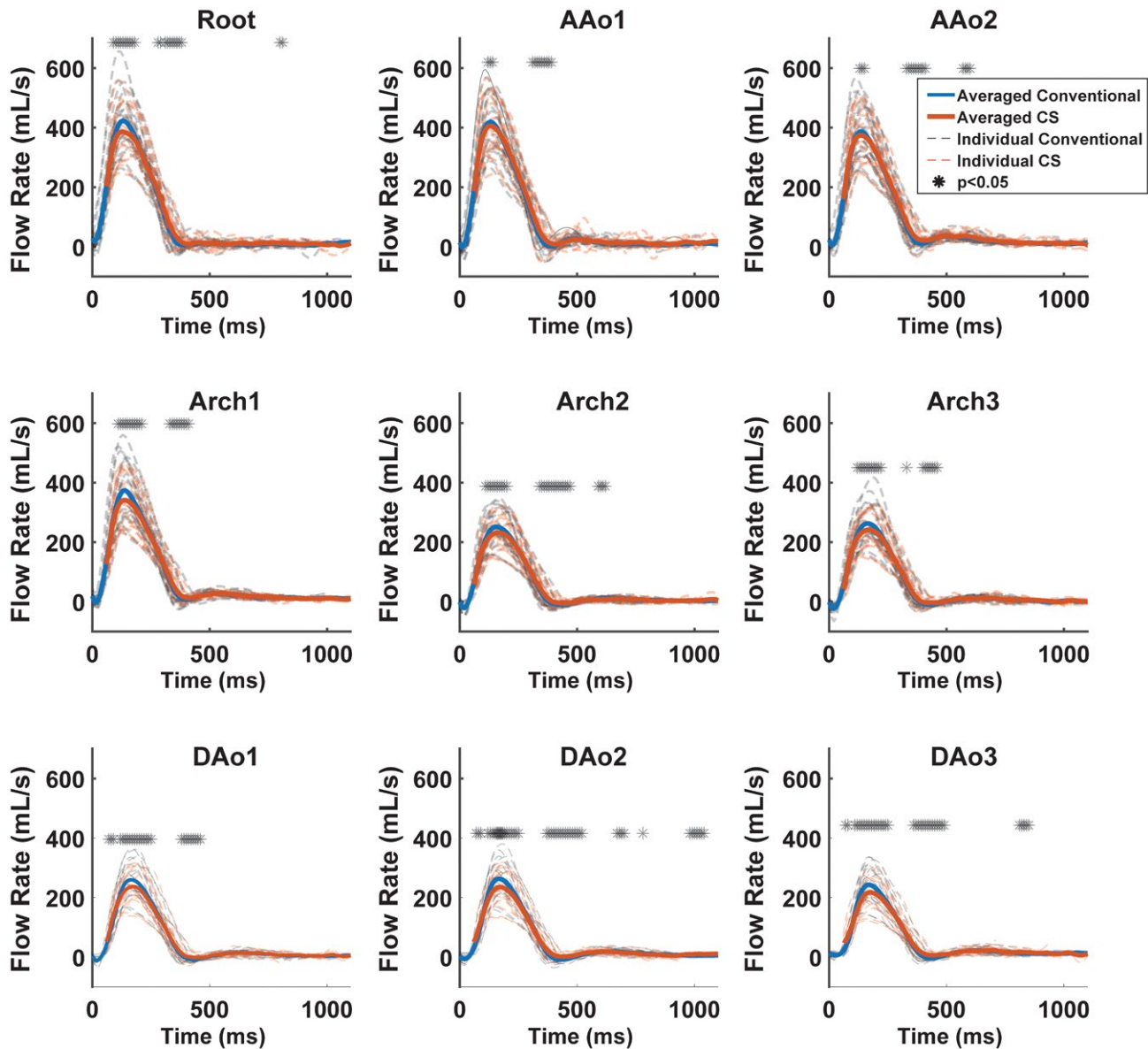


FIGURE 5 Flow-time curves of all 20 healthy volunteers for all 9 2D analysis planes. Solid orange and blue lines represent flow curves averaged over all 20 subjects for CS and conventional 4D flow, respectively. Dotted black and red lines represent flow curves for each individual volunteer. (*) above the curves represent time points with significant differences ($P < 0.05$) between the conventional and CS accelerated 4D flow acquisitions. Good agreement between conventional and CS 4D flow derived flow-time curves as well as mild underestimation of Q_{\max} by CS accelerated 4D flow can be clearly appreciated. Most pronounced differences were found at areas of peak flow or transitions to diastole

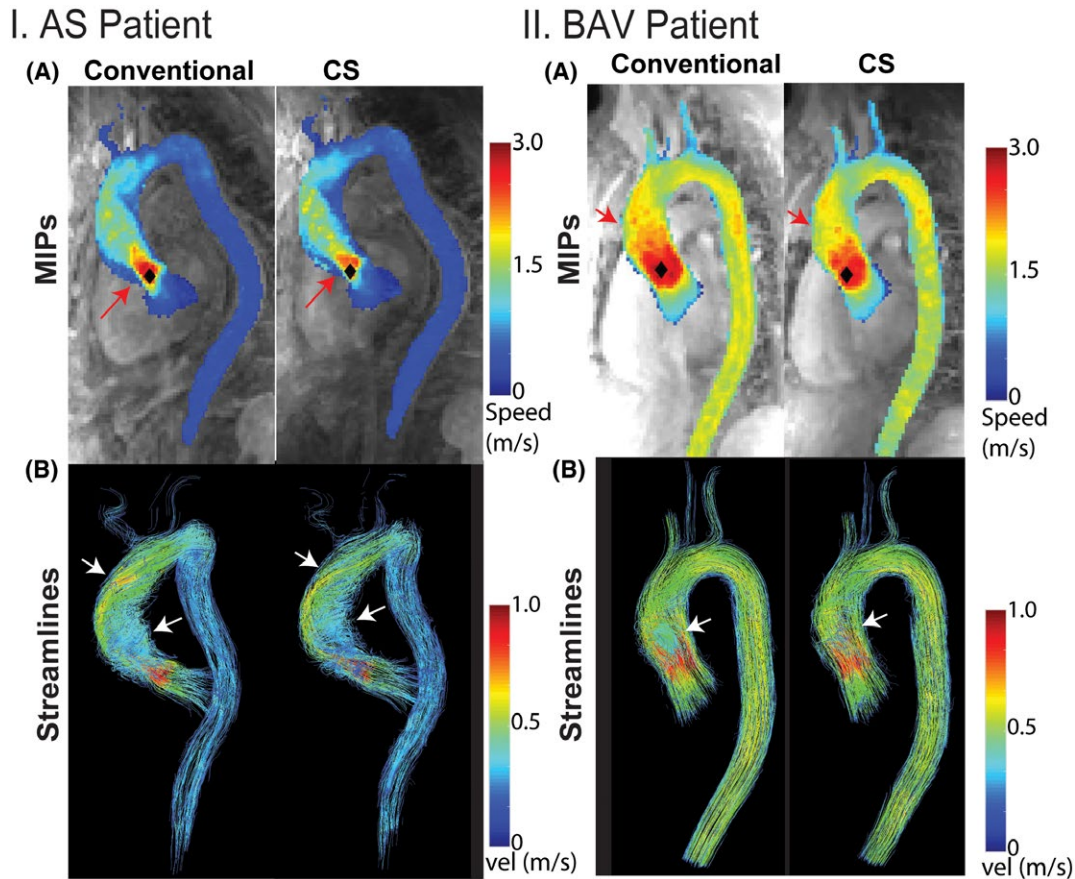


FIGURE 6 Representative in vivo aortic hemodynamics for two patients (I-II) Peak velocity maximum intensity projections (A) and systolic 3D streamlines (B) of conventional 4D flow (GRAPPA, $R = 2$) and CS 4D flow ($R = 7.7$). Black diamonds represent points of maximum velocity in the MIPs. Arrows indicate regions with visible differences between the two techniques. Note the underestimation in areas of high velocities in the ascending and descending aorta (red arrows). Systolic streamlines depict complex helical flow in both techniques, with less dense streamlines in the CS accelerated 4D flow (white arrows)

DAo: 1.31 ± 0.25 m/s; CS, AAo: 1.38 ± 0.17 m/s, Arch: 1.07 ± 0.19 m/s, DAo: 1.10 ± 0.23 m/s, $P < 0.001$).

Voxel-by-voxel comparison between CS and conventional 4D flow velocities across all 20 subjects revealed good agreement with small mean differences (-0.007 ± 0.007 m/s) and LOAs (LOA = 0.154 ± 0.0256 m/s). CS mean velocity over all time points and all phases in the entire aorta was 0.233 ± 0.028 m/s and GRAPPA mean velocity of 0.241 ± 0.029 m/s. A CV of $33.4\% \pm 2.2\%$ indicates some variation in the data. In addition, correlation analysis demonstrated strong and significant relationships between CS accelerated and conventional 4D flow MRI, with a -4% deviation from unity (slope = 0.96 ± 0.036 ; intercept = 0.003 ± 0.005 cm/s; ICC = 0.93 ± 0.02 ; $P < 0.01$ for all volunteers).

3.3 | Patient cohort

CS 4D flow with $R = 7.7$ and conventional 4D flow data were successfully acquired in 11 patients with aortic valve disease in $1:50 \pm 0:25$ min and $7:13 \pm 2:39$ min ($P < 0.001$), respectively. Root plane data for one patient with BAV disease and concurrent

aortic stenosis were excluded from Root plane analysis due to severe velocity aliasing in the ascending aorta that could not be corrected using an anti-aliasing algorithm. 3D blood flow visualization using diastolic streamlines and systolic velocity MIPs in a patient with a prosthetic aortic valve (Figure 4.II) indicate that CS and conventional 4D flow captured similar hemodynamic patterns (Figure 4.II.A), with systolic MIPs depicting high velocity outflow jets, and diastolic streamlines depicting complex recirculating helical flow throughout the entire aorta. Figure 6 depicts two additional patient examples demonstrating depiction of eccentric flow patterns (helical flow and aberrant recirculation) using both CS and conventional methods.

Cumulative flow and velocity quantification across all 11 patients is summarized in Table 3 and Figure 7. v_{\max} values were significantly underestimated by CS compared with conventional 4D flow, in the Arch and DAo, $P < 0.05$ (Conventional, AAo: 3.06 ± 1.21 m/s; Arch: 1.35 ± 0.33 m/s; DAo: 1.09 ± 0.23 m/s; CS, AAo: 2.86 ± 0.91 m/s; Arch: 1.19 ± 0.23 m/s; DAo: 1.00 ± 0.26 m/s). v_{\max} values were significantly greater in patients than volunteers in the AAo when comparing both conventional 4D flow- and CS-derived

TABLE 3 Average volunteer ($n = 20$) and patient ($n = 11$) Q_{\max} and Q_{net} over all planes with corresponding % change in CS values relative to conventional 4D flow (GRAPPA, $R = 2$)

Volunteers ($n = 20$)									
Peak flow, Q_{\max} (mL/s)									
Root*	AAoI*	AAo2*	ArchI*	Arch2*	Arch3*	DAoI*	DAo2*	DAo3*	
GRAPPA	428 ± 98	426 ± 96	393 ± 92	379 ± 94	257 ± 55	270 ± 65	265 ± 57	268 ± 63	249 ± 58
CS R = 7.7	393 ± 82	412 ± 90	378 ± 85	345 ± 81	237 ± 53	245 ± 557	243 ± 53	237 ± 58	222 ± 50
% Change CS	-7.6 ± 5.6	-2.9 ± 6.7	-3.5 ± 7.1	-8.7 ± 4.9	-7.8 ± 6.8	-9.0 ± 6.7	-8.4 ± 6.4	-11.6 ± 6.2	-10.6 ± 5.1
Net flow, Q_{net} (mL/s)									
GRAPPA	82 ± 17	83 ± 17	84 ± 18	79 ± 18	51 ± 12	53 ± 13	53 ± 12	55 ± 13	53 ± 13
CS R = 7.7	83 ± 16	86 ± 17	86 ± 16	77 ± 17	50 ± 11	52 ± 13	52 ± 12	53 ± 12	53 ± 12
% Change CS	1.7 ± 7.6	3.3 ± 8.2	3.5 ± 7.6	-2.1 ± 5.0	-1.6 ± 10.1	-0.8 ± 7.3	-1.7 ± 6.9	-2.9 ± 5.4	-0.6 ± 5.9
Patients ($n = 11$)									
Peak flow, Q_{\max} (mL/s)									
Root	AAoI	AAo2	ArchI*	Arch2*	Arch3	DAoI*	DAo2*	DAo3*	
GRAPPA	444 ± 141	426 ± 109	426 ± 119	405 ± 102	248 ± 63	260 ± 67	269 ± 85	260 ± 74	253 ± 78
CS R = 7.7	449 ± 145	436 ± 113	441 ± 107	370 ± 92	231 ± 63	257 ± 66	244 ± 75	236 ± 70	219 ± 71
% Change CS	1.1 ± 9.2	6.2 ± 10.4	7.2 ± 11.5	-6.3 ± 7.0	-5.9 ± 7.6	1.4 ± 10.7	-5.8 ± 5.5	-6.8 ± 6.9	-10.2 ± 9.4
Net flow, Q_{net} (mL/s)									
Root	AAoI	AAo2	ArchI	Arch2*	Arch3	DAoI	DAo2	DAo3	
GRAPPA	82 ± 17	80 ± 21	81 ± 22	79 ± 18	48 ± 11	46 ± 9	47 ± 10	49 ± 10	49 ± 10
CS R = 7.7	77 ± 27	86 ± 27	90 ± 26	74 ± 19	44 ± 94	48 ± 9	45 ± 8	48 ± 11	49 ± 12
% Change CS	1.4 ± 12.5	7.1 ± 12.4	13.1 ± 20.5	-6.1 ± 9.8	-7.7 ± 8.9	3.6 ± 11.9	-3.7 ± 7.5	-1.0 ± 7.6	0.9 ± 8.1

Abbreviations: AAo, ascending aorta; DAo, descending aorta.
*Significant differences between CS accelerated and conventional 4D flow MRI ($P < 0.05$). AAo = Ascending Aorta, DAo = Descending Aorta.

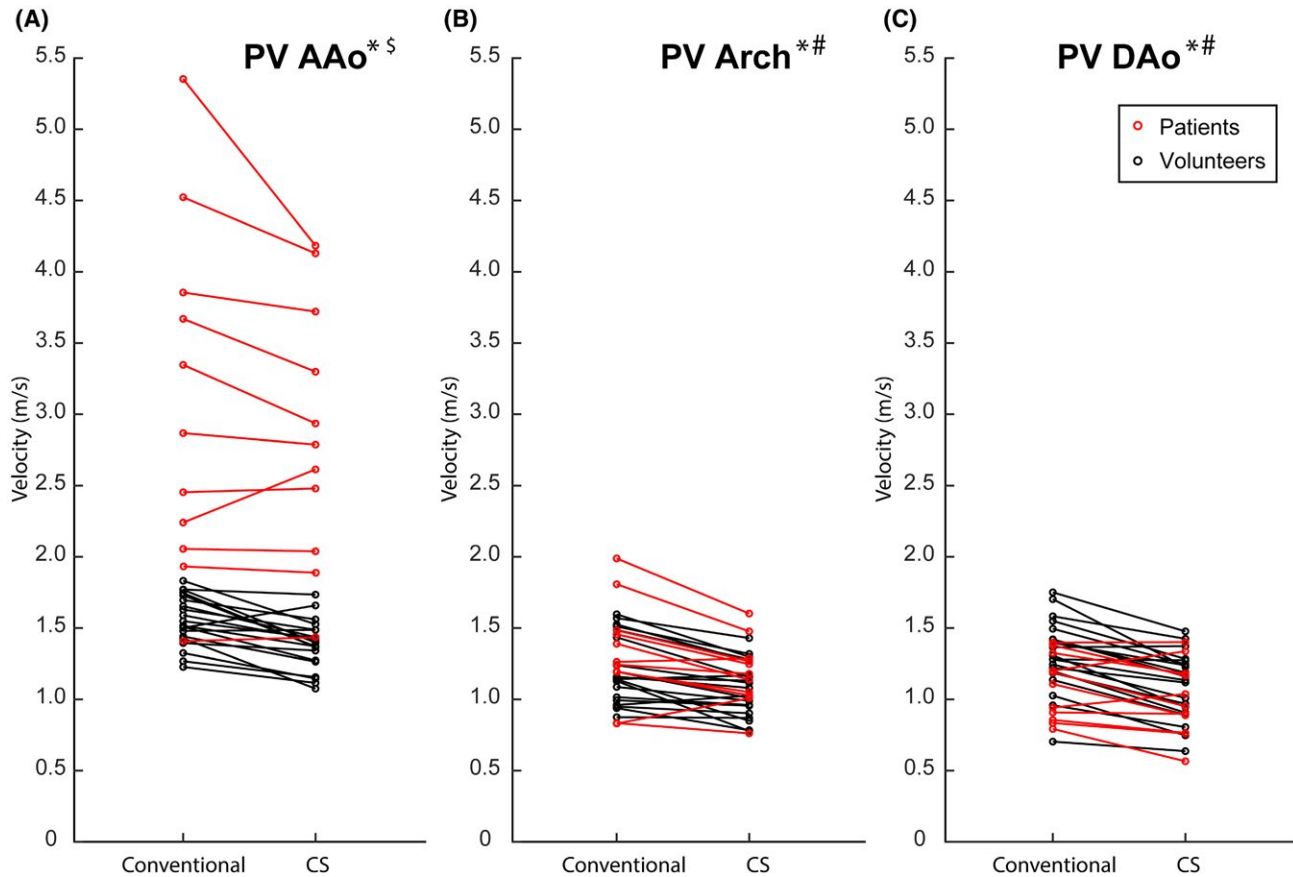


FIGURE 7 Peak velocities for conventional and CS 4D flow over all patients and volunteers in the ascending aorta (AAo), arch, and descending aorta (DAo). Graphs demonstrate the underestimation of velocities in the CS 4D flow in all three regions of interest. Most patients (red circles) had some form of aortic stenosis due to their various aortic valve pathologies; thus, their v_{\max} were higher than those of the volunteers in the AAo. *Significant differences between CS and conventional in volunteers. # Significant differences between CS and conventional in patients. \$ Significant differences between volunteers and patients

values ($P < 0.02$). Q_{net} differed significantly between the methods in the Arch2 ($P = 0.02$), with a -7.7% difference from conventional 4D flow. Q_{max} was significantly decreased in Arch1, Arch2, and DAo1-3 ($P < 0.03$).

Voxel-by-voxel analysis of aortic velocities across all 11 patients revealed good agreement between techniques, with CS mean velocity = 0.272 ± 0.057 m/s and GRAPPA mean velocity = 0.274 ± 0.060 m/s, and a mean difference of -0.002 ± 0.01 m/s and 0.233 ± 0.083 m/s LOA. A CV of $33.9\% \pm 4.7\%$ indicated similar but slightly higher inter- and intra-patient variability compared with volunteers. Correlation analysis revealed a strong correlation between conventional and CS 4D flow with greater correlation analysis SDs compared with the volunteers (slope = 0.958 ± 0.035 ; intercept = 0.011 ± 0.011 m/s; ICC = 0.89 ± 0.08 ; $P < 0.01$).

4 | DISCUSSION

While the utility of 4D flow MRI in evaluating cardiovascular pathologies has long been investigated and supported, its

clinical adoption is typically hindered by long scan times and complicated reconstruction workflows. Here, we developed a highly accelerated 4D flow technique using ReCAR combined with pseudo random undersampling and L1-regularized wavelet-based compressed sensing. Images were reconstructed directly at the MRI scanner in less than 5 min without interrupting clinical workflow. The feasibility and performance of this technique was assessed in vitro, on an aortic coarctation pulsatile flow phantom, as well as in 20 healthy volunteers and 11 patients with various aortic diseases. We have demonstrated that (1) CS 4D flow MRI enabled significant and substantial acceleration of an aortic 4D flow acquisition (~ 2 min versus 7-12 min); (2) full image reconstruction on the scanner in < 5 min allowed for immediate analysis and interpretation; (3) voxel-by-voxel velocity comparison between CS and standard CS 4D flow MRI demonstrated good-excellent agreement; and (4) CS 4D flow MRI demonstrated underestimation of Q_{max} and v_{\max} within 5-13% while maintaining good agreement between methods with regard to Q_{net} ($< 3.5\%$).

In vitro experiments demonstrated that the use of CS with both spatial and temporal undersampling and regularization

predictably led to an underestimation of hemodynamic parameters when compared with conventional GRAPPA acceleration (-13.1% to 2.7% deviation from GRAPPA Q_{\max} , -22.4% to 1.3% difference in v_{\max} over all acceleration factors) as well as some blunting of time-resolved cross-vessel velocity profiles. Reduction in temporal fidelity with CS can also be seen in the time-resolved flow curves (Figure 2B), where the peaks and transitions to diastole (600–800 ms) appear to be slightly blunted in the CS reconstruction. CS underestimation was generally more severe with acceleration factors above 10.2. However, even the maximum evaluated acceleration of $R = 14.1$ resulted in good-to-excellent qualitative and quantitative evaluation of hemodynamics compared with conventional 4D flow (similar systolic flow patterns, flow curves follow similar shapes).

Velocity profiles plotted along a line show consistent velocity profiles between conventional 4D flow and CS 4D flow at different acceleration factors, but some blunting of velocity peaks, suggesting a loss of spatial information potentially due to spatial regularization. Consistent flow patterns, lack of bulk motion, and the overall stability of the in vitro experiment allowed for ideal conditions for a voxel-by-voxel comparison, which further support the finding that good agreement exists between the techniques. In vivo studies demonstrated similar results, with volunteer v_{\max} and Q_{\max} generally within 13% of conventional 4D-flow derived values. In patients with aortic valve disease, variability and relative differences (%) compared with conventional 4D flow were higher than in volunteers.

This result could be explained by the heterogeneity of the patient cohort. While all patients had a history of aortic valve disease, the indications for imaging ranged from aortic valve replacement, to severe aortic stenosis, to aortic insufficiency. In addition, 4D flow is inherently limited by the need to set a velocity sensitivity (Venc). In patients with aortic valve stenosis, a higher Venc (up to 500 cm/s) was needed to capture high peak velocities at the root and AAO. As a result, increased velocity noise coupled with the CS reconstruction could potentially account for the larger deviations in Q_{net} and v_{\max} in these patients. Nonetheless, it is important to note that deranged aortic flow patterns associated with aortic valve disease could be captured in these patients with CS 4D flow (Figures 4, 6, 7). For example, patients with aortic valve disease presented with significantly increased ascending aortic v_{\max} for both CS and conventional 4D flow MRI.

Other studies have also explored the combination of advanced imaging acceleration techniques and 4D flow MRI, including radial sampling schemes (PC-VIPR¹⁰) and multidimensional k-t accelerated parallel imaging schemes (k-t BLAST¹¹, PEAK-GRAPPA¹², k-t PCA¹³). Supporting Information Table S3 provides a concise summary of findings from this study compared with recent publications investigating highly accelerated 4D flow MRI, including MR

imaging parameters and most relevant findings. For example, radial imaging with 3D PC vastly undersampled isotropic projection reconstruction (PC-VIPR) allowed high acceleration factors while maintaining good image quality.³⁸ PC-VIPR studies using acceleration factors ranging from 17 to 61 demonstrated good agreement with 2D PC MRI both in vitro and in vivo ($R^2 = 0.99$ and $R^2 = 0.97$, respectively), but a 6% underestimation in flow in in vitro experiments using a pump with a known flow rate.

K-t PCA is another technique that has been applied to accelerate 4D flow. Values derived from this technique were found to be highly correlated with those of 2D PC MRI ($R^2 = 0.93$ for stroke volumes), with some underestimation in Q_{\max} in the AAO, superior vena cava, main pulmonary artery, and the left and right pulmonary arteries ($-5.1\% \pm 7.5\%$) in volunteers when using an acceleration factor of 8.³⁹ More recently, Bollache et al explored a 2-min aortic protocol using no respiratory navigation, k-t PEAK GRAPPA acceleration ($R = 5$) with variable sampling patterns, and found underestimation in Q_{\max} and v_{\max} (Peak velocity, in vitro, -22% to -0.8% underestimation, in vivo [volunteers], -18% to 6.4% ; *current study*: in vitro, -22.5% to -3.7% , in vivo [volunteers], -16.2% to -9.4%).⁴⁰

These studies both used a similar in vitro set up, and underestimations could be explained by undersampling in the temporal dimension. However, Q_{\max} values were generally larger in the current in vivo study, potentially because of the younger age of the volunteers, and the placement of the quantification planes. Moreover, while both studies incorporated free-breathing 4D flow techniques, Bollache focused on incorporating optimized sampling patterns into a previously developed k-t accelerated parallel imaging technique with the aim to avoid navigator-gating, while the current study focused on incorporating navigator-gating into a k-t accelerated technique using CS. Respiratory-motion effects and the smaller volunteer sample size could explain the higher SDs seen in Bollache's in vivo data. It should also be noted that many of the other 4D flow acceleration techniques summarized in Supporting Information Table S3 have been compared with 2D PC-MRI as the reference for flow imaging, a technique that in itself has been shown to underestimate flow parameters.⁴¹

Other groups have also reported on the combination of CS with 4D flow MRI and found similar underestimations in hemodynamic parameters. One of the first CS 4D flow studies by Hsiao et al successfully applied CS 4D flow MRI using a variable-density Poisson-disk sampling pattern to a pediatric population.²⁵ However, this study focused on using 4D flow to qualitatively characterize cardiac shunts and valvular insufficiency, and no direct comparison was made with conventional 4D flow methods. Dyvorne et al successfully applied CS 4D flow using spiral sampling patterns to acquire abdominal 4D flow data in 24 heartbeats during a

single breath-hold.²⁴ Spiral 4D flow reconstruction took ~3 h per subject offline on a dedicated computer. This group quantified 18 major abdominal vessels and found a significant underestimation in Q_{\max} and v_{\max} in CS compared with Cartesian 4D flow (see Supporting Information Table S3). The increased severity of the underestimation may be due to the small size of abdominal vessels, which are likely more difficult to segment and limited by fewer voxels per region of interest than the thoracic aorta used in our study.

More recently, Cheng et al successfully applied CS 4D flow using a radial view-ordering (VDRad) design, where Cartesian ky-kz samples were ordered in variable-density spiral-like spokes, to pediatric patients with congenital heart anomalies with acceleration rates of 10.6 and offline reconstructions of ~1 h.^{42,43} While Cheng's studies focused on comparing sampling patterns or flexibility in clinical applications due to flexible data binning and reconstruction schemes, the authors did note a lower average flow rate in their XD flow recon using 4 temporal bins (~0.25 L/min) compared with their unbinned 4D flow (temporally averaged, ~0.35 L/min).

While the aforementioned studies suggest that temporal undersampling is a factor in the underestimation of peak hemodynamic parameters, CS reconstructions may benefit from the exploration of data redundancy and sparsity in the velocity encoding dimension. Rich et al. recently developed a Bayesian approach to allow 4D flow imaging of the aortic valve in a single breath-hold (24 heartbeats).²¹ This study explored incoherency in the spatial, temporal, and velocity-encoding directions and demonstrated that the unique structure of 4D flow MRI data can be exploited by incorporating the velocity encodings as another data dimension. This study found that ReVEAL4D consistently outperformed L1-SENSE, which does not incorporate temporal acceleration, but is comparable to kt SPARSE-SENSE at low acceleration rates, and outperforms kt SPARSE-SENSE at high acceleration rates ($R > 15$) of up to 27. These computationally intense techniques using higher dimension datasets are becoming more feasible as both offline and inline computing power improves.

The main limitation of this study is the low number of subjects. Patient evaluations were limited to a heterogeneous group of patients and a small overall sample size. In addition, 1 patient had significant velocity aliasing in the ascending aorta. While most of this could be corrected, there was residual aliasing that affected the area of the plane at the aortic root; thus, this patient's data were left out of the averaged flow and statistical analyses for the plane at the aortic root. Although the results are encouraging, further patient studies are warranted to identify the limitations of this technique and potential implementation improvements, as well as protocol changes that could alleviate differences from conventional 4D flow. For example, patients with complex hemodynamics who could benefit from examination of smaller branching vessels may require different spatial or temporal

regularization compared with the protocol that we developed based on healthy controls, or perhaps they may benefit greatly from an improved spatial resolution.

Because some of the patients received Gd-contrast, further exploration of the differences between contrast and noncontrast protocols may improve CS 4D flow results. Moreover, voxel-by-voxel comparisons may be limited by patient movement. While CS and conventional 4D flow scans were sequentially acquired and matched in spatial coverage and visually compared for agreement, single voxel movement could influence the value of the reported voxel-by-voxel parameters. Thus, voxel-by-voxel evaluation was included as only one aspect of hemodynamic evaluation. Moreover, an acceleration factor of 7.7 was chosen based on phantom experiments for all subsequent in vivo studies. While testing multiple acceleration factors in vivo is preferable, it is difficult to fit these into allotted patient and volunteer scan times.

CS 4D flow at $R = 7.7$ produced peak flow and velocity values within 13% of conventional methods. While this difference may not be acceptable for all clinical scenarios, this initial study demonstrates the feasibility of a highly accelerated 4D flow method that can capture similar aortic hemodynamics in both patients and volunteers. This study provides a foundation for an improved 4D flow workflow, with further investigation into improved agreement with conventional 4D flow. Future work will explore more acceleration factors to find the limits of the protocol, exploration of the velocity encode dimension in the CS reconstruction, a test-retest study, evaluation of image quality, evaluation in different applications (e.g., intracardiac, abdominal, neurovascular), and further exploration of the protocol itself (e.g., acceleration factors, Venc, resolution).

5 | CONCLUSIONS

In conclusion, we have demonstrated that aortic 4D flow MRI with ReCAR, variable-density phyllotaxis undersampling, and CS is feasible in 2 min of acquisition time with less than 5 min of reconstruction on the scanner. With short acquisition time and inline reconstruction, it is a promising approach to incorporate 4D flow into the standard clinical workflow as a screening tool to provide comprehensive 3D hemodynamic information of the aorta.

ORCID

Liliana E. Ma  <https://orcid.org/0000-0001-8834-8519>

REFERENCES

1. Dyverfeldt P, Bissell M, Barker AJ, et al. 4D flow cardiovascular magnetic resonance consensus statement. *J Cardiovasc Magn Reson*. 2015;17:72.

2. Stankovic Z, Allen BD, Garcia J, Jarvis KB, Markl M. 4D flow imaging with MRI. *Cardiovasc Diagn Ther*. 2014;4:173.
3. Roldán-Alzate A, Francois CJ, Wieben O, Reeder SB. Emerging applications of abdominal 4D flow MRI. *AJR Am J Roentgenol*. 2016;207:58–66.
4. Markl M, Frydrychowicz A, Kozerke S, Hope M, Wieben O. 4D flow MRI. *J Magn Reson Imaging*. 2012;36:1015–1036.
5. Bissell MM, Hess AT, Biasioli L, et al. Aortic dilation in bicuspid aortic valve disease: flow pattern is a major contributor and differs with valve fusion type. *Circ Cardiovasc Imaging*. 2013;6:499–507.
6. Frydrychowicz A, Markl M, Hirtler D, et al. Aortic hemodynamics in patients with and without repair of aortic coarctation: in vivo analysis by 4D flow-sensitive magnetic resonance imaging. *Invest Radiol*. 2011;46:317–325.
7. Guzzardi DG, Barker AJ, Van Ooij P, et al. Valve-related hemodynamics mediate human bicuspid aortopathy: insights from wall shear stress mapping. *J Am Coll Cardiol*. 2015;66:892–900.
8. Hope MD, Hope TA, Crook SE, et al. 4D flow CMR in assessment of valve-related ascending aortic disease. *JACC: Cardiovasc Imaging*. 2011;4:781–787.
9. Mahadevia R, Barker AJ, Schnell S, et al. Bicuspid aortic cusp fusion morphology alters aortic three-dimensional outflow patterns, wall shear stress, and expression of aortopathy. *Circulation*. 2014;129:673–682.
10. Johnson KM, Lum DP, Turski PA, Block WF, Mistretta CA, Wieben O. Improved 3D phase contrast MRI with off-resonance corrected dual echo VIPR. *Magn Reson Med*. 2008;60:1329–1336.
11. Baltes C, Kozerke S, Hansen MS, Pruessmann KP, Tsao J, Boesiger P. Accelerating cine phase-contrast flow measurements using k-t BLAST and k-t SENSE. *Magn Reson Med*. 2005;54:1430–1438.
12. Jung B, Ullmann P, Honal M, Bauer S, Hennig J, Markl M. Parallel MRI with extended and averaged GRAPPA kernels (PEAK-GRAPPA): optimized spatiotemporal dynamic imaging. *J Magn Reson Imaging*. 2008;28:1226–1232.
13. Giese D, Schaeffter T, Kozerke S. Highly undersampled phase-contrast flow measurements using compartment-based k-t principal component analysis. *Magn Reson Med*. 2013;69:434–443.
14. Feng L, Axel L, Chandarana H, Block KT, Sodickson DK, Otazo R. XD-GRASP: Golden-angle radial MRI with reconstruction of extra motion-state dimensions using compressed sensing. *Magn Reson Med*. 2016;75:775–788.
15. Feng L, Grimm R, Block KT, et al. Golden-angle radial sparse parallel MRI: combination of compressed sensing, parallel imaging, and golden-angle radial sampling for fast and flexible dynamic volumetric MRI. *Magn Reson Med*. 2014;72:707–717.
16. Feng L, Srichai MB, Lim RP, et al. Highly accelerated real-time cardiac cine MRI using k-t SPARSE-SENSE. *Magn Reson Med*. 2013;70:64–74.
17. Kim D, Dyvorner HA, Otazo R, Feng L, Sodickson DK, Lee VS. Accelerated phase-contrast cine MRI using k-t SPARSE-SENSE. *Magn Reson Med*. 2012;67:1054–1064.
18. Lustig M, Donoho D, Pauly JM. Sparse MRI: the application of compressed sensing for rapid MR imaging. *Magn Reson Med*. 2007;58:1182–1195.
19. Feng L, Coppo S, Piccini D, et al. 5D whole-heart sparse MRI. *Magn Reson Med*. 2018;79:826–838.
20. Tariq U, Hsiao A, Alley M, Zhang T, Lustig M, Vasanawala SS. Venous and arterial flow quantification are equally accurate and precise with parallel imaging compressed sensing 4D phase contrast MRI. *J Magn Reson Imaging*. 2013;37:1419–1426.
21. Rich A, Potter LC, Jin N, Liu Y, Simonetti OP, Ahmad R. A Bayesian approach for 4D flow imaging of aortic valve in a single breath-hold. *Magn Reson Med*. 2019;81:811–824.
22. Jin N, Ma L, Chow K, et al. Highly-accelerated 4D flow in the aorta with compressed sensing, respiratory controlled adaptive k-space reordering and inline reconstruction. In: Proceedings of the 26th Annual Meeting of the ISMRM, Paris, France, 2018. Abstract 0687.
23. Ma LE, Chow K, Forman C, et al. Highly accelerated 4D flow with compressed sensing for evaluation of aortic hemodynamics. In: Proceedings of the 30th Annual Meeting of the Society for Magnetic Resonance Angiography, Glasgow, Scotland, 2018. Abstract 27.
24. Dyvorner H, Knight-Greenfield A, Jajamovich G, et al. Abdominal 4D flow MR imaging in a breath hold: combination of spiral sampling and dynamic compressed sensing for highly accelerated acquisition. *Radiology*. 2014;275:245–254.
25. Hsiao A, Lustig M, Alley MT, Murphy MJ, Vasanawala SS. Evaluation of valvular insufficiency and shunts with parallel-imaging compressed-sensing 4D phase-contrast MR imaging with stereoscopic 3D velocity-fusion volume-rendered visualization. *Radiology*. 2012;265:87–95.
26. Bailes D, Gilderdale D, Bydder G, Collins A, Firmin D. Respiratory ordered phase encoding (ROPE): a method for reducing respiratory motion artefacts in MR imaging. *J Comput Assist Tomogr*. 1985;9:835–838.
27. Markl M, Harloff A, Bley TA, et al. Time-resolved 3D MR velocity mapping at 3T: improved navigator-gated assessment of vascular anatomy and blood flow. *J Magn Reson Imaging*. 2007;25:824–831.
28. Uecker M, Lai P, Murphy MJ, et al. ESPIRiT—an eigenvalue approach to autocalibrating parallel MRI: where SENSE meets GRAPPA. *Magn Reson Med*. 2014;71:990–1001.
29. Forman C, Piccini D, Grimm R, Hutter J, Hornegger J, Zenge MO. High-resolution 3D whole-heart coronary MRA: a study on the combination of data acquisition in multiple breath-holds and 1D residual respiratory motion compensation. *MAGMA*. 2014;27:435–443.
30. Wetzl J, Forman C, Wintersperger BJ, et al. High-resolution dynamic CE-MRA of the thorax enabled by iterative TWIST reconstruction. *Magn Reson Med*. 2017;77:833–840.
31. Beck A, Teboulle M. A fast iterative shrinkage-thresholding algorithm for linear inverse problems. *SIAM J Imaging Sci*. 2009;2:183–202.
32. Liu J, Rapin J, T-c Chang, et al. Dynamic cardiac MRI reconstruction with weighted redundant Haar wavelets. In: Proceedings of the 20th Annual Meeting of ISMRM, Melbourne, Australia, 2012. Abstract 4249.
33. Lorenz R, Benk C, Bock J, et al. Closed circuit MR compatible pulsatile pump system using a ventricular assist device and pressure control unit. *Magn Reson Med*. 2012;67:258–268.
34. Bock J, Kreher B, Hennig J, Markl M. Optimized pre-processing of time-resolved 2D and 3D phase contrast MRI data. In: Proceedings of the 15th Annual Meeting of ISMRM, Berlin, Germany, 2007. Abstract 3138.
35. Busch J, Giese D, Kozerke S. Image-based background phase error correction in 4D flow MRI revisited. *J Magn Reson Imaging*. 2017;46:1516–1525.
36. Walker PG, Cranney GB, Scheidegger MB, Waseleski G, Pohost GM, Yoganathan AP. Semiautomated method for noise reduction and background phase error correction in MR phase velocity data. *J Magn Reson Imaging*. 1993;3:521–530.

37. Rose MJ, Jarvis K, Chowdhary V, et al. Efficient method for volumetric assessment of peak blood flow velocity using 4D flow MRI. *J Magn Reson Imaging*. 2016;44:1673–1682.
38. Gu T, Korosec FR, Block WF, et al. PC VIPR: a high-speed 3D phase-contrast method for flow quantification and high-resolution angiography. *AJNR Am J Neuroradiol*. 2005;26:743–749.
39. Giese D, Wong J, Greil GF, Buehrer M, Schaeffter T, Kozerke S. Towards highly accelerated Cartesian time-resolved 3D flow cardiovascular magnetic resonance in the clinical setting. *J Cardiovasc Magn Reson*. 2014;16:42.
40. Bollache E, Barker AJ, Dolan RS, et al. k-t accelerated aortic 4D flow MRI in under two minutes: feasibility and impact of resolution, k-space sampling patterns, and respiratory navigator gating on hemodynamic measurements. *Magn Reson Med*. 2018;79:195–207.
41. Bollache E, van Ooij P, Powell A, Carr J, Markl M, Barker AJ. Comparison of 4D flow and 2D velocity-encoded phase contrast MRI sequences for the evaluation of aortic hemodynamics. *Int J Cardiovasc Imaging*. 2016;32:1529–1541.
42. Cheng JY, Hanneman K, Zhang T, et al. Comprehensive motion-compensated highly accelerated 4D flow MRI with ferumoxylol enhancement for pediatric congenital heart disease. *J Magn Reson Imaging*. 2016;43:1355–1368.
43. Cheng JY, Zhang T, Alley MT, et al. Comprehensive multi-dimensional MRI for the simultaneous assessment of cardiopulmonary anatomy and physiology. *Sci Rep*. 2017;7:5330.
44. Jenkinson M, Smith S. A global optimisation method for robust affine registration of brain images. *Med Image Anal*. 2001;5:143–156.

SUPPORTING INFORMATION

Additional supporting information may be found online in the Supporting Information section at the end of the article.

FIGURE S1 In vivo voxel alignment was ensured in two steps: 1) Consecutive acquisition of the conventional and CS scans and the use of the same spatial coverage (field of view and voxel size) to ensure minimal patient movement between scans. 2) Visual inspection of the overlaid 3D visualization of masks from the CS visualization as well as the conventional

GRAPPA acquisition. For all subjects, overlaid masks before registration appeared to match well. Registration was attempted using FLIRT registration,⁴⁴ but in all cases, there was no improvement with registration. Registered masks appeared to agree slightly less in all cases. Singular voxel shifts are difficult to avoid in in vivo data and may affect analysis results, thus, the voxel-by-voxel analysis was only one component of the analysis

TABLE S1 Voxel-by-voxel phantom comparison of absolute velocities. Bland-Altman analysis is presented with the mean difference and limits of agreement (LOA). CV = coefficient of variation. (*) depicts significance of $P < 0.001$ for correlation analyses of ICC

TABLE S2 Voxel-by-voxel phantom comparison of absolute velocities for all three velocity directions (x,y,z). Absolute velocities were used. Note increased CV compared with speed analysis in table S1, but relatively low mean difference and correlation close to 1. This may be due to the consideration of all time points within the entire segmentation. Values within low velocities (Y,Z -direction) may be particularly susceptible to noise. Bland-Altman analysis is presented with the mean difference and limits of agreement (LOA). CV = coefficient of variation. (*) depicts significance of $P < 0.001$ for correlation analyses of ICC

TABLE S3 Previous evaluations in the literature of accelerated 4D flow MRI. Reconstruction times are included if noted in the paper. v_{\max} = peak velocity, Q_{\max} = peak flow, SR = spatial resolution, Temp. Res. = temporal resolution, Recon. = reconstruction

How to cite this article: Ma LE, Markl M, Chow K, et al. Aortic 4D flow MRI in 2 minutes using compressed sensing, respiratory controlled adaptive k-space reordering, and inline reconstruction. *Magn Reson Med*. 2019;00:1–16. <https://doi.org/10.1002/mrm.27684>